

# Mapping charge excitations in generalized Wigner crystals

Received: 27 October 2022

Accepted: 18 December 2023

Published online: 29 January 2024


 Check for updates

Hongyuan Li<sup>1,2,3,8</sup>, Ziyu Xiang<sup>1,2,3,8</sup>, Emma Regan<sup>1,2,3</sup>, Wenyu Zhao<sup>1</sup>, Renee Sailus<sup>4</sup>, Rounak Banerjee<sup>4</sup>, Takashi Taniguchi<sup>5</sup>, Kenji Watanabe<sup>6</sup>, Sefaattin Tongay<sup>4</sup>, Alex Zettl<sup>1,3,7</sup>, Michael F. Crommie<sup>1,3,7</sup>  & Feng Wang<sup>1,3,7</sup> 

Transition metal dichalcogenide-based moiré superlattices exhibit strong electron–electron correlations, thus giving rise to strongly correlated quantum phenomena such as generalized Wigner crystal states. Evidence of Wigner crystals in transition metal dichalcogenide moiré superlattices has been widely reported from various optical spectroscopy and electrical conductivity measurements, while their microscopic nature has been limited to the basic lattice structure. Theoretical studies predict that unusual quasiparticle excitations across the correlated gap between upper and lower Hubbard bands can arise due to long-range Coulomb interactions in generalized Wigner crystal states. However, the microscopic proof of such quasiparticle excitations is challenging because of the low excitation energy of the Wigner crystal. Here we describe a scanning single-electron charging spectroscopy technique with nanometre spatial resolution and single-electron charge resolution that enables us to directly image electron and hole wavefunctions and to determine the thermodynamic gap of generalized Wigner crystal states in twisted WS<sub>2</sub> moiré heterostructures. High-resolution scanning single-electron charging spectroscopy combines scanning tunnelling microscopy with a monolayer graphene sensing layer, thus enabling the generation of individual electron and hole quasiparticles in generalized Wigner crystals. We show that electron and hole quasiparticles have complementary wavefunction distributions and that thermodynamic gaps of ~50 meV exist for the 1/3 and 2/3 generalized Wigner crystal states in twisted WS<sub>2</sub>.

A Wigner crystal is the crystalline phase of electrons stabilized at low electron density when long-range Coulomb interactions dominate over quantum fluctuations in electron motion<sup>1</sup>. The recent discovery of flat moiré minibands in van der Waals heterostructures has opened

a new route to realize Wigner crystal states at zero magnetic field<sup>2–9</sup>. A variety of generalized Wigner crystal states have been reported in transition metal dichalcogenide moiré superlattices<sup>2–6,10</sup>, and real-space imaging of the electron lattice of generalized Wigner crystals has

<sup>1</sup>Department of Physics, University of California at Berkeley, Berkeley, CA, USA. <sup>2</sup>Graduate Group in Applied Science and Technology, University of California at Berkeley, Berkeley, CA, USA. <sup>3</sup>Materials Sciences Division, Lawrence Berkeley National Laboratory, Berkeley, CA, USA. <sup>4</sup>School for Engineering of Matter, Transport and Energy, Arizona State University, Tempe, AZ, USA. <sup>5</sup>International Center for Materials Nanoarchitectonics, National Institute for Materials Science, Tsukuba, Japan. <sup>6</sup>Research Center for Functional Materials, National Institute for Materials Science, Tsukuba, Japan. <sup>7</sup>Kavli Energy NanoScience Institute at the University of California at Berkeley and the Lawrence Berkeley National Laboratory, Berkeley, CA, USA. <sup>8</sup>These authors contributed equally: Hongyuan Li, Ziyu Xiang.  e-mail: [crommie@physics.berkeley.edu](mailto:crommie@physics.berkeley.edu); [fengwang76@berkeley.edu](mailto:fengwang76@berkeley.edu)

been performed using a new form of non-invasive scanning tunneling microscopy (STM) imaging<sup>6</sup>. A microscopic understanding of elementary excitations in generalized Wigner crystal, however, is still lacking. Theoretical studies predict that unusual quasiparticle excitations across the correlated gap between upper and lower Hubbard bands can arise due to long-range Coulomb interactions in generalized Wigner crystal states<sup>8,11,12</sup>. However, because of the fragile electron lattice and small energy scale, it is challenging to image quasiparticle (for example, electron/hole) wavefunctions and to spectroscopically determine the correlated gaps of generalized Wigner crystals.

Several scanning probe microscopy techniques have previously been developed to probe fragile correlated states, such as scanning charge accumulation microscopy<sup>13–15</sup> and scanning single-electron transistor microscopy<sup>16–18</sup>. The spatial resolution of these microscopy tools, however, is typically limited to  $\sim 100$  nm, and therefore is not sufficient to image generalized Wigner crystal quasiparticle states at the single-unit-cell level.

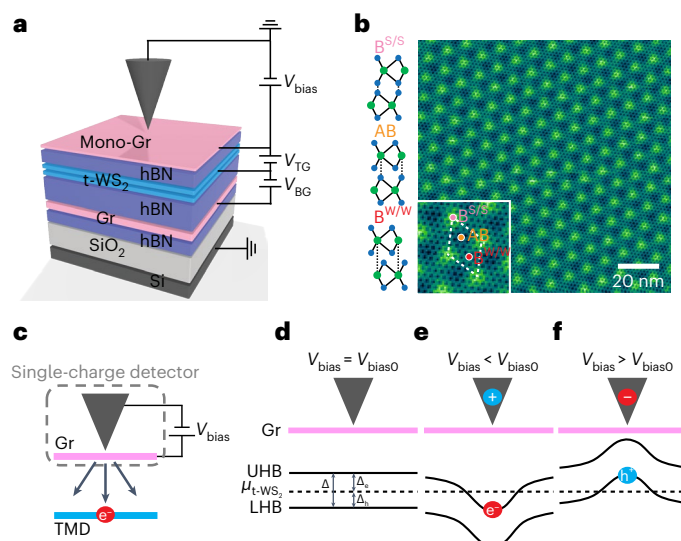
Here we describe a scanning single-electron charging (SSEC) spectroscopy that has  $\sim 1$  nm spatial resolution and single-electron sensitivity. SSEC spectroscopy combines STM with a monolayer graphene sensing layer and enables local manipulation of individual electron and hole quasiparticles in generalized Wigner crystals via STM tip-based local gating. It enables direct visualization of quasiparticle excitations and spectroscopic determination of the thermodynamic gap of generalized Wigner crystals. Using this technique, we observe that electron- and hole-quasiparticle excitations exhibit complementary wavefunction distributions and that thermodynamic gaps of  $\sim 50$  meV exist for the  $1/3$  and  $2/3$  generalized Wigner crystal states.

## SSEC measurement

Figure 1a shows the design of the sample and the measurement scheme. The sample is a near- $60^\circ$  twisted bilayer  $WS_2$  ( $t$ - $WS_2$ ) moiré heterostructure encapsulated in hexagonal boron nitride (hBN) layers. It is dual gated by a monolayer of graphene on top (top gate) and graphite on the bottom (bottom gate). The hBN dielectric layer thicknesses for the top and bottom gates are 5.8 nm and 37 nm, respectively. Sample fabrication details are included in Methods. The charge carrier densities of the  $t$ - $WS_2$  and the top graphene sensing layer are tuned independently by applying a bottom gate voltage  $V_{BG}$  and a top gate voltage  $V_{TG}$ . A bias voltage ( $V_{bias}$ ) is applied between the graphene top gate (otherwise known as the sensing layer) and the STM tip. Application of  $V_{bias}$  allows electrons in the  $t$ - $WS_2$  moiré heterostructure to be manipulated by local tip-gating and to be detected through charging events measured via the tunnel current to the graphene sensing layer.

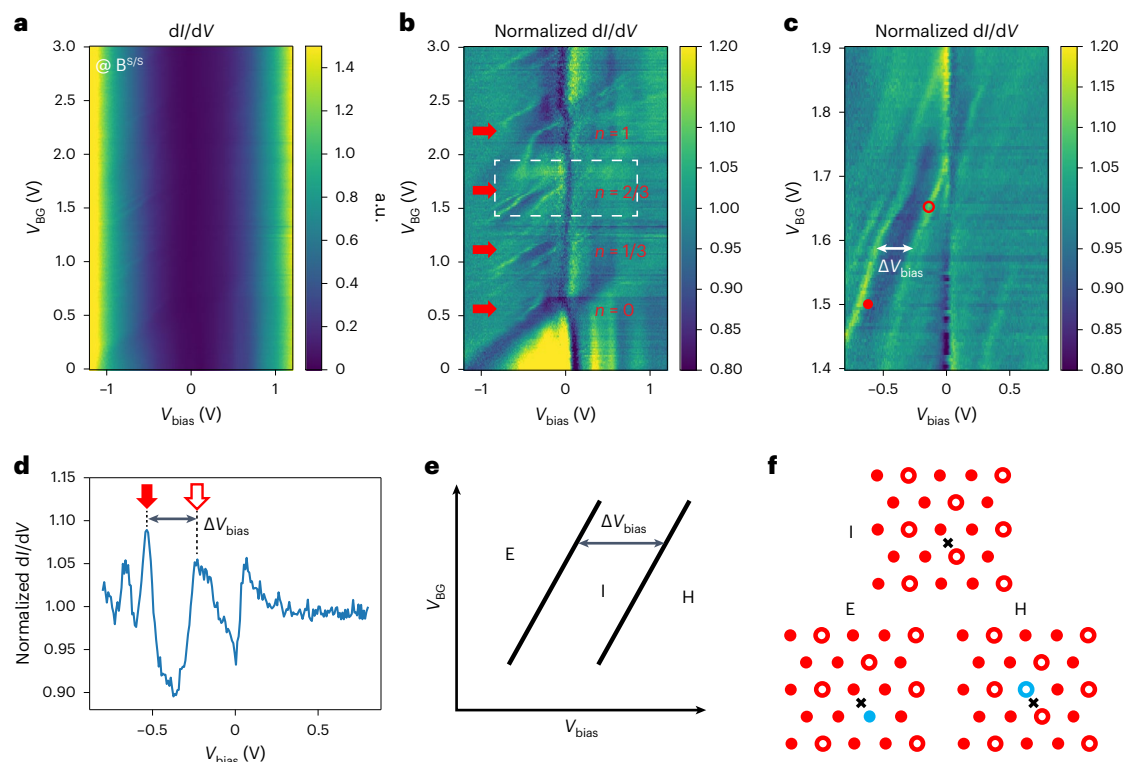
Conventional STM measurement of the graphene sensing layer provides information on the corrugation of the heterostructure sample as shown in Fig. 1b. The thin top graphene and hBN bend conformally and thus inherit the topography of the  $t$ - $WS_2$  moiré superlattice. Two sets of moiré superlattices with distinct periods are observed. The larger periodicity (9 nm) originates from the  $t$ - $WS_2$  moiré superlattice which has a twist angle of  $58^\circ$ , while the smaller periodicity ( $\sim 1.5$  nm) corresponds to the moiré superlattice formed by the top graphene and hBN which has a twist angle of  $9.6^\circ$ . The  $58^\circ$   $t$ - $WS_2$  moiré superlattice exhibits a triangular lattice with three types of high-symmetry stacking regions in each unit cell: a bright region ( $B^{S/S}$  stacking), a dark region (AB stacking) and a medium height region ( $B^{W/W}$  stacking)<sup>19</sup> (Fig. 1b, inset). The bonding arrangements of the  $B^{S/S}$ , AB and  $B^{W/W}$  stacking orders are sketched on the left side of Fig. 1b.

Figure 1c–f illustrates the dual role of the STM tip in SSEC spectroscopy. In Fig. 1c the biased STM tip is seen to act as a local gate on the  $t$ - $WS_2$  because its electrical field partially penetrates the monolayer graphene. This is because graphene has a small electron density of states and weak screening, especially when its Fermi level is near the Dirac point. When the sample-tip bias  $V_{bias} = V_{bias0}$ , where  $V_{bias0}$  is a small offset bias voltage that cancels the work function difference between



**Fig. 1 | SSEC measurement of a  $t$ - $WS_2$  moiré superlattice. a**, Schematic of the dual-gated  $t$ - $WS_2$  moiré superlattice device. The top hBN thickness (5 nm) is slightly smaller than the moiré lattice constant (9 nm). Top gate ( $V_{TG}$ ) and bottom gate ( $V_{BG}$ ) voltages are separately applied to independently control the carrier densities in the  $t$ - $WS_2$  superlattice and top graphene (Gr) sensing layer. **b**, A typical large-scale topography image of the top graphene layer ( $V_{bias} = -0.62$  V,  $I = 150$  pA). Three different stacking regions are labelled in the close-up image in the inset:  $B^{S/S}$  stacking (pink dots), AB stacking (yellow dots) and  $B^{W/W}$  stacking (red dots). The structures of the  $B^{S/S}$ , AB and  $B^{W/W}$  stacking are illustrated in the left panel. **c**, Illustration of SSEC spectroscopy. The electric field from the tip bias partially penetrates the graphene and induces quasiparticle excitations in the  $t$ - $WS_2$ . The tip–graphene tunnel junction detects changes in the number of electrons in the  $t$ - $WS_2$  due to long-range Coulomb interactions. TMD, transition metal dichalcogenide. **d–f**, Illustration of tip-induced quasiparticle excitation in correlated insulator for  $V_{bias} = V_{bias0}$  (**d**),  $V_{bias} < V_{bias0}$  (**e**) and  $V_{bias} > V_{bias0}$  (**f**), where  $V_{bias0}$  is the offset bias voltage that cancels the work function difference between the tip and the top graphene sensing layer. Solid curves represent the lower Hubbard band (LHB) and upper Hubbard band (UHB), and the dashed line represents the chemical potential  $\mu_{t-WS_2}$ . **d**, For  $V_{bias} = V_{bias0}$ , the LHB and UHB are uniform. **e**, For large  $V_{bias} < V_{bias0}$ , the UHB is pushed beneath  $\mu_{t-WS_2}$  by tip-gating, inducing a local electron excitation. **f**, For large  $V_{bias} > V_{bias0}$ , tip-gating induces a local hole excitation.

the tip and the graphene, the tip exerts no local gating effect (Fig. 1d). With a decreased (increased)  $V_{bias}$ , positive (negative) charge accumulates at the tip apex and generates local band bending in the  $t$ - $WS_2$  due to the electric field penetrating through the monolayer graphene (Fig. 1e,f). With sufficiently strong band bending, a single electron (hole) quasiparticle will be injected into the  $t$ - $WS_2$ . The added charge due to this tip-induced quasiparticle excitation will, in turn, alter the tip–graphene tunnel current via long-range Coulomb interactions (discussed further in Supplementary Information, section 2). SSEC spectroscopy has some similarity to capacitance spectroscopy in that the tip bias voltage drives charging of the  $t$ - $WS_2$ . However, unlike conventional capacitance spectroscopy, SSEC spectroscopy locally manipulates individual electrons/holes in the heterostructure and is responsive to individual charge excitation through the tunnel current to the graphene sensing layer. A spatial resolution of  $\sim 1$  nm can be achieved in SSEC spectroscopy for thin top hBN layers having a thickness of several nanometres. It also shares similarities with the tip-induced charging behaviour in molecules and quantum dots observed in previous scanning probe measurements<sup>20–25</sup>. However, the SSEC spectroscopy enables a quantitative thermodynamic measurement of correlated electrons, which is beyond the capability of previous single-electron charging studies. The key difference lies in the application of the graphene sensing layer, which not only decouples the



**Fig. 2 | Scanning tunnelling spectroscopy study of quasiparticle excitations in generalized Wigner crystals.** **a**,  $dI/dV$  spectra of the graphene sensing layer as a function of sample-tip bias ( $V_{\text{bias}}$ ) and bottom gate voltage ( $V_{\text{BG}}$ ) (measured with the tip held over the t-WS<sub>2</sub> B<sup>S/S</sup> site).  $V_{\text{TG}}$  is fixed at 0.52 V. **b**, Normalized form of the  $dI/dV$  spectra shown in **a**. The  $dI/dV$  spectrum at each  $V_{\text{BG}}$  is normalized by the averaged  $dI/dV$  spectrum for all  $V_{\text{BG}}$  values (see Supplementary Information, section 1, for details). Dispersive bright lines corresponding to  $dI/dV$  peaks are clustered around the filling factors  $n = 0, 1/3, 2/3, 1$  (labelled in red). **c**, High-resolution  $dI/dV$  spectra corresponding to the  $n = 2/3$  state measured over the range enclosed by the white box in **b**. Two bright dispersive lines with similar slopes exist on opposite sides of the  $n = 2/3$  state and correspond to electron charging events (solid dot) and hole charging events (open circle). The  $\Delta V_{\text{bias}}$

offset between them is marked in white. **d**,  $dI/dV$  line cut of **c** at  $V_{\text{BG}} = 1.60$  V shows peaks corresponding to dispersive features in **c** labelled with a solid arrow (electron charging) and an open arrow (hole charging) that are offset from each other by  $\Delta V_{\text{bias}}$ . **e**, Schematic showing the charging regimes of the t-WS<sub>2</sub> moiré superlattice near the  $n = 2/3$  state. I, intrinsic generalized Wigner crystal insulator phase; E, electron excitation regime; H, hole excitation regime. The charging regimes are separated by two dispersive lines in the  $V_{\text{BG}}-V_{\text{bias}}$  parameter space that are offset from each other by  $\Delta V_{\text{bias}}$ . **f**, Real-space sketch of the I, E and H regimes. Electron-filled sites (solid dots) and empty sites (open circles) of the  $n = 2/3$  generalized Wigner crystal as shown. Tip-induced electron excitation is marked by a solid blue dot and hole excitation by a blue open circle. The black cross labels the tip position.

single-charge excitation and tunnelling current measurement but also minimizes the tip perturbation while retaining a high spatial resolution.

## Spectroscopic evidence of quasiparticle excitations in generalized Wigner crystals

Figure 2a shows the bottom gate voltage ( $V_{\text{BG}}$ ) dependence of the  $dI/dV$  spectra of the tip-graphene tunnel junction when the tip is placed over the B<sup>S/S</sup> site of the moiré unit cell (see Supplementary Information, section 6, for stacking site dependence of the  $dI/dV$  spectra). We started by setting the top gate voltage to  $V_{\text{TG}} = 0.52$  V, which shifts the t-WS<sub>2</sub> chemical potential up to the conduction band edge while keeping the graphene Fermi level close to the Dirac point<sup>6</sup>. Under these conditions increasing  $V_{\text{BG}}$  increases the global electron doping in the t-WS<sub>2</sub> layers. The resulting  $dI/dV$  measurement of the sensing layer is dominated by a broad increase in the  $dI/dV$  signal for increased  $V_{\text{bias}}$  regardless of polarity, which mostly reflects the local density of states of graphene and does not show an obvious dependence on  $V_{\text{BG}}$  (that is, on the t-WS<sub>2</sub> doping). The impact of electrical charge added to the t-WS<sub>2</sub> moiré superlattice is better seen by normalizing the  $dI/dV$  spectra at each  $V_{\text{BG}}$  by the averaged  $dI/dV$  spectrum over all  $V_{\text{BG}}$  values as seen in Fig. 2b (see Supplementary Information, section 1, for normalization details). This normalization removes the broad rising background and reveals multiple dispersive bright lines that correspond to peaks in  $dI/dV$  that shift in energy with applied  $V_{\text{BG}}$ . These peaks are clustered around several electron doping levels in the t-WS<sub>2</sub> moiré superlattice

(that is, different  $V_{\text{BG}}$  values), as denoted by horizontal arrows in Fig. 2b. Their  $V_{\text{BG}}$  values correspond to t-WS<sub>2</sub> electron filling factors of  $n = 0, 1/3, 2/3, 1$  (as labelled in red), where  $n$  is the number of electrons per moiré site. The filling factors shown here are based on carrier densities extracted using the device capacitance as described in ref. 6. Our SSEC imaging (Supplementary Information, section 3, and Fig. 3) is also consistent with these filling factors.

The  $dI/dV$  spectra in Fig. 2b show two or more dispersive lines clustered around each correlated insulating state at  $n = 1/3, 2/3$ , and 1. To better understand this behaviour, Fig. 2c shows higher-resolution  $V_{\text{BG}}$ -dependent  $dI/dV$  spectra near the  $n = 2/3$  generalized Wigner crystal state (the phase space inside the white dashed box in Fig. 2b). Two bright dispersive lines with similar slope as well as several weaker features nearby move together through the  $V_{\text{BG}}$  region associated with the  $n = 2/3$  state. It should be noted that the  $V_{\text{BG}}$ -independent vertical peaks and dips around  $V_{\text{bias}} = 0$  in Fig. 2b,c are artefacts due to the numerical normalization. Figure 2d displays a horizontal line cut of Fig. 2c at  $V_{\text{BG}} = 1.60$  V, where clear  $dI/dV$  peaks (labelled with vertical arrows) can be observed at the  $V_{\text{bias}}$  positions of the bright lines in Fig. 2c. These  $dI/dV$  peaks do not mark the energy locations of resonances in the local density of states, but rather arise from electron and hole charging events in the generalized Wigner crystal states of t-WS<sub>2</sub>.

To understand this, we look to the sketch in Fig. 2e that illustrates the charging diagram of the t-WS<sub>2</sub> moiré superlattice in the  $n = 2/3$  state. There are three different regimes as shown in Fig. 2f: the ‘intrinsic’



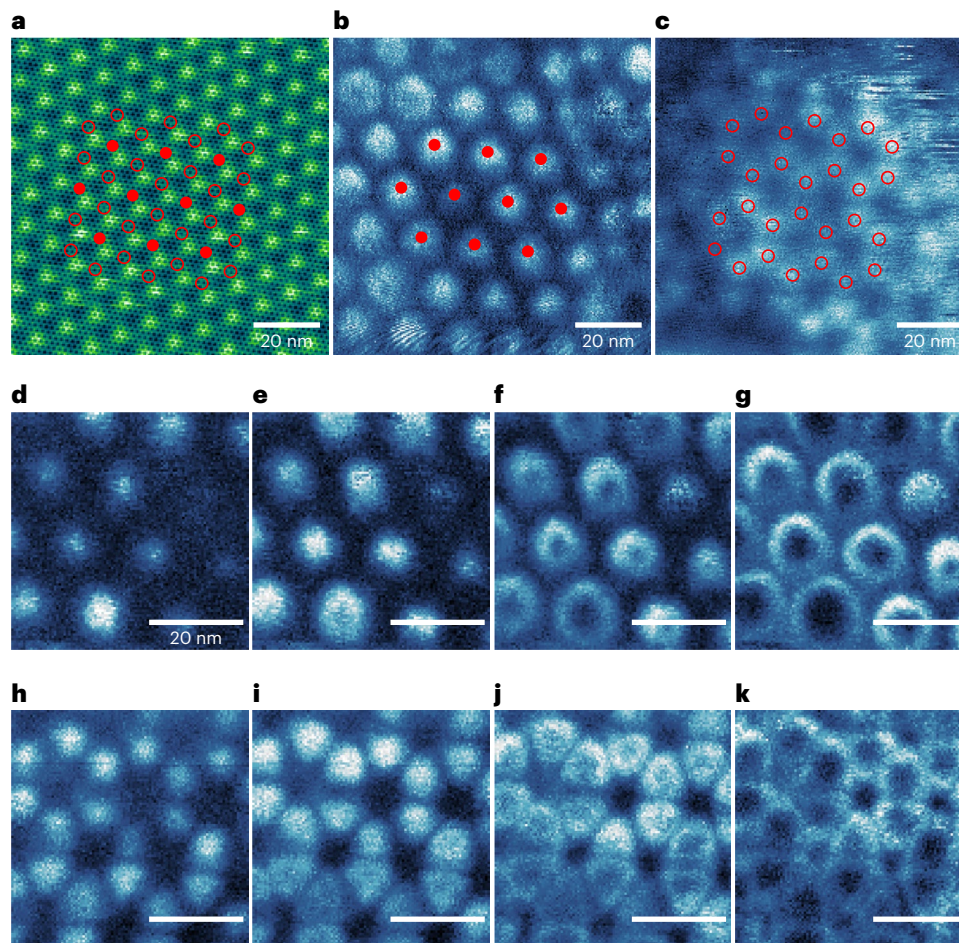


**Fig. 3 | Mapping electron and hole excitations of the  $n = 2/3$  generalized Wigner crystal.** **a**, STM topography image of the graphene sensing layer showing the t-WS<sub>2</sub> moiré superlattice ( $V_{\text{bias}} = -0.59$  V,  $I = 150$  pA). **b**,  $dI/dV$  map of the same area shown in **a** for applied voltages corresponding to the electron excitation boundary ( $V_{\text{BG}} = 1.50$  V,  $V_{\text{TG}} = 0.52$  V,  $V_{\text{bias}} = -0.59$  V). Sites of electron excitations are marked with solid red dots. **c**,  $dI/dV$  map of the same area shown in **a** for voltages corresponding to the hole excitation boundary ( $V_{\text{BG}} = 1.65$  V,  $V_{\text{TG}} = 0.52$  V,  $V_{\text{bias}} = -0.14$  V). Sites of hole excitations are marked with open circles. **d–g**, Evolution of  $dI/dV$  maps of the electron charging peak of the  $n = 2/3$  state

with increasingly negative  $V_{\text{bias}}$ :  $-0.66$  V (**d**),  $-0.68$  V (**e**),  $-0.71$  V (**f**),  $-0.73$  V (**g**) ( $V_{\text{TG}} = 0.52$  V,  $V_{\text{BG}} = 1.50$  V). The electron charging signals widen into a growing circle at each moiré site as  $V_{\text{bias}}$  becomes more negative. **h–k**, Evolution of  $dI/dV$  maps of the hole charging peak of the  $n = 2/3$  state with increasingly positive  $V_{\text{bias}}$ :  $0.20$  V (**h**),  $0.22$  V (**i**),  $0.24$  V (**j**),  $0.26$  V (**k**) ( $V_{\text{TG}} = 0.49$  V,  $V_{\text{BG}} = 1.90$  V). The hole charging signal widens into a growing circle as  $V_{\text{bias}}$  becomes more positive. The solid dots in **b** and open circles in **c** are overlaid in **a** and are seen to be perfectly complementary. **d–k** share the same scale bar.

generalized Wigner crystal insulator phase (I) (solid red dots mark the locations of electrons in the moiré unit cell while open circles mark empty cells), the electron excitation regime (E) where an electron (blue solid dot in Fig. 2f) is injected below the tip at a large negative  $V_{\text{bias}}$ , and the hole excitation regime (H) where a hole (blue open circle in Fig. 2f) is injected at a large positive  $V_{\text{bias}}$ . These regimes are separated by two dispersive lines in the  $V_{\text{BG}}-V_{\text{bias}}$  parameter space in Fig. 2e with the slope of the dispersive lines being determined by the efficiency of the tip as an effective top gate relative to chemical potential shifts induced by the bottom gate. Starting from the intrinsic regime (for example, Fig. 1d), a reduction of  $V_{\text{bias}}$  causes the tip to become positively charged. Crossing the boundary from I to E corresponds to pushing the UHB energetically below the t-WS<sub>2</sub> chemical potential  $\mu_{\text{t-WS}_2}$  and locally inducing an electron charging event (Fig. 1e). Similarly, if  $V_{\text{bias}}$  is increased and crosses the boundary from I to H, then the LHB is energetically pushed above  $\mu_{\text{t-WS}_2}$ , resulting in a local hole charging event (Fig. 1f). These charge excitations alter the tunnel junction conductance and result in a peak in the  $dI/dV$  spectra (discussed further in Supplementary Information, section 2). The dispersive  $dI/dV$  peaks in Fig. 2b,c correspond to the electron/hole excitation boundaries sketched in Fig. 2e. The reason that the intrinsic region does not bracket  $V_{\text{bias}} = 0$  is

most likely because of the work function difference between the tip and the graphene sensing layer. Additional weaker  $dI/dV$  peak features observed in Fig. 2c at higher positive (negative)  $V_{\text{bias}}$  correspond to the injection of additional electrons and holes at nearby moiré cells adjacent to the tip location.

### Mapping electron and hole excitations of the generalized Wigner crystal

To establish our assignment of the features seen in Fig. 2 as electron and hole excitations of the generalized Wigner crystal, we directly image these charging events using SSEC spectroscopy. Figure 3a displays an STM topography image of a highly defect-free t-WS<sub>2</sub> moiré region chosen for imaging electron/hole excitations. Figure 3b shows a  $dI/dV$  map measured over this same area at  $V_{\text{BG}} = 1.50$  V,  $V_{\text{TG}} = 0.52$  V and  $V_{\text{bias}} = -0.59$  V, which corresponds to the electron excitation boundary denoted by the filled circle in Fig. 2c. A triangular lattice of bright dots is seen with a period larger than the underlying moiré superlattice by a factor of  $\sqrt{3}$ . This new triangular lattice reflects the wavefunction distribution of the excited electron in the generalized  $n = 2/3$  Wigner crystal. To confirm that this pattern originates from tip-induced electron excitations we tested how it evolves with  $V_{\text{bias}}$ . A typical aspect of

charging features is ‘ring expansion’ with increased bias<sup>20–25</sup> because the tip can then induce charging events from more distant positions. Figure 3d–g shows the evolution of the charging rings with increasing  $|V_{\text{bias}}|$ , obtained at  $V_{\text{BG}} = 1.50$  V and  $V_{\text{TG}} = 0.52$  V. The electron charging signal at the different moiré unit cells is seen to expand into a wide charging ring with increasingly negative  $V_{\text{bias}}$ , precisely as expected for electron injection.

Figure 3c shows a  $dI/dV$  map taken at the hole excitation boundary for  $n = 2/3$  filling, corresponding to the open circle in Fig. 2c ( $V_{\text{BG}} = 1.65$  V,  $V_{\text{TG}} = 0.52$  V,  $V_{\text{bias}} = -0.14$  V). A honeycomb lattice of bright dots (open circles) here reflects the wavefunction of hole excitations in this generalized Wigner crystal. The tip bias dependence of this pattern also confirms its origin as shown in Fig. 3h–k. Here the hole charging signal in the different moiré unit cells is seen to expand into a wider charging ring for increasingly positive  $V_{\text{bias}}$ . Note that in Fig. 3h–k  $V_{\text{TG}}$  is set at 0.49 V instead of the original 0.52 V so that a non-zero hole charging signal can be observed over a wider  $V_{\text{bias}}$  range (extending to the positive  $V_{\text{bias}}$  side), and hence we can measure the continuous evolution of the charging rings as a function of  $V_{\text{bias}}$  (the  $V_{\text{TG}}$  dependence of the  $dI/dV$  spectra is discussed in Supplementary Information, section 5).

The complementarity of the electron and hole excitation wavefunctions of the generalized Wigner crystal state can be seen by overlaying the hollow circles and solids dots of Fig. 3b,c onto the topography of Fig. 3a. Both the hollow and solid circles are seen to be localized in the  $B^{\text{W/W}}$  stacking regions, where the lowest-energy conduction moiré flat bands are predicted to reside<sup>19</sup>. The electron excitation distribution (red dots) and the hole excitation distribution (open circles) combine perfectly to yield the full moiré superlattice. Hole excitations correspond precisely to the filled electron locations for an  $n = 2/3$  generalized Wigner crystal (that is, a honeycomb lattice), whereas electron excitations occur at the hollow centres of the honeycomb lattice. This is the pattern that one might intuitively expect from classical electrostatic reasoning.

Since the thermodynamic gap of a correlated state is the chemical potential difference for adding a single hole or electron, it is possible to extract the thermodynamic gap of generalized Wigner crystals from our SSEC spectra. To see this we define the energy difference between the chemical potential and LHB as  $\Delta_{\text{h}}$  (Fig. 1d), and the bias applied to the tip to create a hole excitation as  $V_{\text{h}}$ . We then write  $\Delta_{\text{h}} = \alpha_{\text{h}} e V_{\text{h}}$ , where  $\alpha_{\text{h}}$  is a geometric constant defined by the tip-gating efficiency when the tip is above a hole site ( $e$  is the charge of an electron). Similarly, we can write  $\Delta_{\text{e}} = \alpha_{\text{e}} (-e) V_{\text{e}}$  where  $\Delta_{\text{e}}$  is the energy difference between the chemical potential and UHB, and the factors  $V_{\text{e}}$  and  $\alpha_{\text{e}}$  are defined for electron excitations. If  $\alpha_{\text{e}} = \alpha_{\text{h}} = \alpha$ , then the thermodynamic gap,  $\Delta = \Delta_{\text{e}} + \Delta_{\text{h}}$ , can be written as

$$\Delta = ae(V_{\text{h}} - V_{\text{e}}) = ae\Delta V_{\text{bias}}, \quad (1)$$

where  $\Delta V_{\text{bias}}$  is the experimental sample-tip bias difference measured between the hole excitation and electron excitation boundaries as shown in Fig. 2c–e (see Supplementary Information, section 7, for more details on the determination of  $\Delta V_{\text{bias}}$ ). A key requirement in this analysis is that the capacitive coupling between the tip and surface is equivalent for electron and hole excitations (that is,  $\alpha_{\text{e}} = \alpha_{\text{h}}$ ). This requirement is satisfied in the measurements shown in Fig. 2 which were performed with the tip positioned above the  $B^{\text{S/S}}$  site in the  $t$ -WS<sub>2</sub> moiré unit cell, which is the same distance to the nearest excited electron or hole.

To obtain a quantitative value of the generalized Wigner crystal thermodynamic gap,  $\Delta$ , we must determine the value of  $\alpha$ . It is also useful to introduce the bottom gate coupling parameter  $\beta$  such that the electric potential change at the  $t$ -WS<sub>2</sub> moiré site is  $\Delta\Phi = e\alpha V_{\text{bias}} - e\beta V_{\text{BG}}$ . The ratio,  $\alpha/\beta$ , is an experimentally accessible quantity since it is the slope of the dispersive features observed in Fig. 2b,c (charging occurs when the  $\Phi$ -dependent UHB or LHB becomes equal to the chemical potential). The value of  $\alpha$  is obtained by the experimentally determined ratio  $\alpha/\beta$

through a one-to-one correspondence between  $\alpha$  and  $\alpha/\beta$ . This correspondence relation between  $\alpha$  and  $\alpha/\beta$  is obtained through numerical simulation of the tip-surface electrostatics (see Supplementary Information, section 4, for simulation details). In the simulation we model the bottom gate as a metallic plate. Due to the unknown geometry of the STM tip, we model the tip in two extreme situations: (1) as a metallic cone and (2) as a metallic sphere. The screening by Dirac electrons in the graphene sensing layer is included in the simulation (see Supplementary Information, section 4, for details). The  $t$ -WS<sub>2</sub> layer is regarded as a thin insulator since it is in a correlated insulating phase. To obtain  $\alpha$ , we monitor the local electric potential change,  $\Delta\Phi$ , in the  $t$ -WS<sub>2</sub> layer that is induced by applying non-zero  $V_{\text{bias}}$ . The main variable parameters in the simulation are the tip geometry (cone angle  $\theta$  for the conic tip model and sphere radius for the spherical tip model) and the tip height ( $h$ ). Although these parameters are hard to obtain experimentally, our simulation results indicate that the correspondence relation between  $\alpha$  and  $\alpha/\beta$  is almost independent of the tip shape and height (Supplementary Fig. 6) where the uncertainty in the correspondence relation due to the unknown tip geometry is less than 3%. With such a tip-geometry-independent correspondence relation, we are thus able to determine  $\alpha = 0.160 \pm 0.005$  from the experimentally measured ratio  $\frac{\alpha}{\beta} = 0.51 \pm 0.01$ . From equation (1) this results in experimental thermodynamic gaps for the  $n = 1/3$ ,  $2/3$  and 1 correlated states of  $\Delta_{n=1/3} = 50 \pm 11$  meV,  $\Delta_{n=2/3} = 45 \pm 11$  meV, and  $\Delta_{n=1} = 106 \pm 29$  meV, respectively (the uncertainty here is calculated from both the standard deviation in our measurement of  $\Delta V_{\text{bias}}$  and the uncertainty of  $\alpha$ ).

## Conclusions

We have demonstrated a non-invasive high-resolution microscopic tool that enables us to induce electron/hole excitations locally in two-dimensional (2D) generalized Wigner crystal systems. This technique allows us to measure the thermodynamic gaps of generalized Wigner crystals having different filling factors and to map their electron and hole excitations. The high spatial resolution of our technique further enables us to map the spatial distribution of the thermodynamic gaps (see examples in Supplementary Information, section 8), which could facilitate the study of how moiré structure and disorders impact the moiré correlated electrons. This technique should be applicable to the characterization of other fragile correlated electron systems.

## Online content

Any methods, additional references, Nature Portfolio reporting summaries, source data, extended data, supplementary information, acknowledgements, peer review information; details of author contributions and competing interests; and statements of data and code availability are available at <https://doi.org/10.1038/s41565-023-01594-x>.

## References

- Wigner, E. On the interaction of electrons in metals. *Phys. Rev.* **46**, 1002–1011 (1934).
- Regan, E. C. et al. Mott and generalized Wigner crystal states in WSe<sub>2</sub>/WS<sub>2</sub> moiré superlattices. *Nature* **579**, 359–363 (2020).
- Xu, Y. et al. Correlated insulating states at fractional fillings of moiré superlattices. *Nature* **587**, 214–218 (2020).
- Huang, X. et al. Correlated insulating states at fractional fillings of the WS<sub>2</sub>/WSe<sub>2</sub> moiré lattice. *Nat. Phys.* **17**, 715–719 (2021).
- Jin, C. et al. Stripe phases in WSe<sub>2</sub>/WS<sub>2</sub> moiré superlattices. *Nat. Mater.* **20**, 940–944 (2021).
- Li, H. et al. Imaging two-dimensional generalized Wigner crystals. *Nature* **597**, 650–654 (2021).
- Wang, L. et al. Correlated electronic phases in twisted bilayer transition metal dichalcogenides. *Nat. Mater.* **19**, 861–866 (2020).
- Pan, H., Wu, F. & Sarma, S. D. Quantum phase diagram of a moiré-Hubbard model. *Phys. Rev. B* **102**, 201104 (2020).

9. Tang, Y. et al. Simulation of Hubbard model physics in  $WSe_2/WS_2$  moiré superlattices. *Nature* **579**, 353–358 (2020).
10. Li, T. et al. Charge-order-enhanced capacitance in semiconductor moiré superlattices. *Nat. Nanotechnol.* **16**, 1068–1072 (2021).
11. Slagle, K. & Fu, L. Charge transfer excitations, pair density waves, and superconductivity in moiré materials. *Phys. Rev. B* **102**, 235423 (2020).
12. Padhi, B., Chitra, R. & Phillips, P. W. Generalized Wigner crystallization in moiré materials. *Phys. Rev. B* **103**, 125146 (2021).
13. Tessmer, S., Glicofridis, P., Ashoori, R., Levitov, L. & Melloch, M. Subsurface charge accumulation imaging of a quantum Hall liquid. *Nature* **392**, 51–54 (1998).
14. Finkelstein, G., Glicofridis, P., Ashoori, R. & Shayegan, M. Topographic mapping of the quantum Hall liquid using a few-electron bubble. *Science* **289**, 90–94 (2000).
15. Steele, G. A., Ashoori, R., Pfeiffer, L. & West, K. Imaging transport resonances in the quantum Hall effect. *Phys. Rev. Lett.* **95**, 136804 (2005).
16. Zondiner, U. et al. Cascade of phase transitions and Dirac revivals in magic-angle graphene. *Nature* **582**, 203–208 (2020).
17. Pierce, A. T. et al. Unconventional sequence of correlated Chern insulators in magic-angle twisted bilayer graphene. *Nat. Phys.* **17**, 1210–1215 (2021).
18. Xie, Y. et al. Fractional Chern insulators in magic-angle twisted bilayer graphene. *Nature* **600**, 439–443 (2021).
19. Naik, M. H. & Jain, M. Ultraflatbands and shear solitons in moiré patterns of twisted bilayer transition metal dichalcogenides. *Phys. Rev. Lett.* **121**, 266401 (2018).
20. Teichmann, K. et al. Controlled charge switching on a single donor with a scanning tunneling microscope. *Phys. Rev. Lett.* **101**, 076103 (2008).
21. Pradhan, N. A., Liu, N., Silien, C. & Ho, W. Atomic scale conductance induced by single impurity charging. *Phys. Rev. Lett.* **94**, 076801 (2005).
22. Brar, V. W. et al. Gate-controlled ionization and screening of cobalt adatoms on a graphene surface. *Nat. Phys.* **7**, 43–47 (2011).
23. Wong, D. et al. Characterization and manipulation of individual defects in insulating hexagonal boron nitride using scanning tunnelling microscopy. *Nat. Nanotechnol.* **10**, 949–953 (2015).
24. Li, H. et al. Imaging local discharge cascades for correlated electrons in  $WS_2/WSe_2$  moiré superlattices. *Nat. Phys.* **17**, 1114–1119 (2021).
25. Stomp, R. et al. Detection of single-electron charging in an individual InAs quantum dot by noncontact atomic-force microscopy. *Phys. Rev. Lett.* **94**, 056802 (2005).

**Publisher's note** Springer Nature remains neutral with regard to jurisdictional claims in published maps and institutional affiliations.

Springer Nature or its licensor (e.g. a society or other partner) holds exclusive rights to this article under a publishing agreement with the author(s) or other rightsholder(s); author self-archiving of the accepted manuscript version of this article is solely governed by the terms of such publishing agreement and applicable law.

© The Author(s), under exclusive licence to Springer Nature Limited 2024



## Methods

### Sample fabrication

The encapsulated t-WS<sub>2</sub> moire heterostructure stack was fabricated using a micromechanical stacking technique<sup>26</sup>. A poly(propylene carbonate (PPC) film stamp was used to pick up all exfoliated 2D material flakes. The 2D material layers in the main heterostructure region were picked up in the following order: substrate hBN, graphite, bottom hBN, first WS<sub>2</sub> monolayer, second monolayer, graphene nanoribbon array (not shown in Fig. 1), top hBN, and then monolayer graphene. The graphene nanoribbon array serves as a contact electrode for the t-WS<sub>2</sub> and is fabricated by an electrode-free local anodic oxidization lithography technique<sup>27</sup>. The two WS<sub>2</sub> monolayers are obtained by cutting an originally complete single flake into two pieces using electrode-free local anodic oxidization to precisely control their crystal directions. The PPC film together with the stacked sample was then peeled, flipped over and transferred onto a Si/SiO<sub>2</sub> substrate (SiO<sub>2</sub> thickness, 285 nm). The PPC layer was subsequently removed using ultrahigh-vacuum annealing at 230 °C, resulting in an atomically clean heterostructure suitable for STM measurements. A 50 nm gold and 5 nm chromium metal layer was evaporated through a shadow mask to form electrical contacts to the graphene layers.

### Scanning tunnelling spectroscopy measurement

A modulation of 25 mV amplitude and 500–900 Hz frequency was applied to the tip bias to obtain the  $dI/dV$  signal.

### Data availability

The data supporting the findings of this study are included in the main text and in the Supplementary Information files, and are also available at <https://github.com/HongyuanLiCMP/Mapping-Charge-Excitations-in-Generalized-Wigner-Crystals>.

## References

26. Wang, L. et al. One-dimensional electrical contact to a two-dimensional material. *Science* **342**, 614–617 (2013).
27. Li, H. et al. Electrode-free anodic oxidation nanolithography of low-dimensional materials. *Nano Lett.* **18**, 8011–8015 (2018).

## Acknowledgements

This work was primarily funded by the US Department of Energy (DOE), Office of Science, Office of Basic Energy Sciences, Materials Sciences

and Engineering Division under contract number DE-AC02-05-CH11231 (van der Waals heterostructure program KCFW16) (device electrode preparation and STM spectroscopy). Support was also provided by the US Army Research Office under MURI award W911NF-17-1-0312 (device layer transfer) and by National Science Foundation (NSF) award DMR-1807233 (surface preparation). S.T. acknowledges support from DOE-SC0020653 (materials synthesis), NSF DMR-1955889 (magnetic measurements), NSF CMMI-1933214, NSF 2206987, NSF ECCS 2052527, DMR 2111812 and CMMI 2129412. K.W. and T.T. acknowledge support from the Elemental Strategy Initiative conducted by the Ministry of Education, Culture, Sports, Science and Technology (MEXT), Japan (grant number JPMXP0112101001), the Japan Society for the Promotion of Science (JSPS) KAKENHI (grant number JP20H00354) and the Core Research for Evolutional Science and Technology (CREST) (JPMJCR15F3), Japan Science and Technology Agency (JST) for bulk hBN crystal growth and analysis.

## Author contributions

H.L., M.F.C. and F.W. conceived the project. H.L. and Z.X. performed the STM measurement. H.L., Z.X., E.R. and W.Z. fabricated the heterostructure device. H.L., Z.X., A.Z., M.F.C. and F.W. discussed the experimental design and analyzed the experimental data. R.S., R.B. and S.T. grew the WS<sub>2</sub> crystals. K.W. and T.T. grew the hBN single crystal. All authors discussed the results and wrote the paper.

## Competing interests

The authors declare no competing interests.

## Additional information

**Supplementary information** The online version contains supplementary material available at <https://doi.org/10.1038/s41565-023-01594-x>.

**Correspondence and requests for materials** should be addressed to Michael F. Crommie or Feng Wang.

**Peer review information** *Nature Nanotechnology* thanks the anonymous reviewer(s) for their contribution to the peer review of this work.

**Reprints and permissions information** is available at [www.nature.com/reprints](http://www.nature.com/reprints).